

NUMERICAL SIMULATION OF STRONGLY SWIRLING TURBULENT FLOWS THROUGH AN ABRUPT EXPANSION

Joongcheol Paik

Department of Civil Engineering,
Kangnung-Wonju National University
120 Gangneung Daehangno, Gangneung, Gangwon, 210-702, Korea
paik@nukw.ac.kr

Fotis Sotiropoulos

St. Anthony Falls Laboratory, Department of Civil Engineering
University of Minnesota
2 Third Avenue SE, Minneapolis, MN 55414, USA
fotis@umn.edu

ABSTRACT

Turbulent swirling incompressible flow through an abrupt axisymmetric expansion is investigated numerically using detached-eddy simulation at Reynolds numbers = 3.0×10^4 and 1.0×10^5 . The effects of swirl intensity on the coherent dynamics of the flow are systematically studied by carrying out numerical simulations over a range of swirl numbers from 0.17 to 1.23. Comparison of the computed solutions with the experimental measurements of Dellenback et al. [AIAA Journal. Vol 26, pp. 669-681] shows that the numerical simulations resolve both the axial and swirl mean velocity and turbulence intensity profiles with very good accuracy. Our simulations show that critical prerequisite for accurate predictions of the flow downstream of the expansion is the specification of inlet conditions at a plane sufficiently far upstream of the expansion in order to avoid the spurious suppression of the low-frequency, large-scale precessing of the vortex core, which occurs in simulations with short inlet segment. Further improvements in the accuracy of the computed solutions can be obtained by moderate mesh refinement. Coherent structure visualizations with the q -criterion and Lagrangian particle tracking are used to elucidate the rich dynamics of the flow as a function of the swirl number with emphasis on the onset of the bubble-type vortex breakdown just downstream of the expansion, strong on-axis recirculation along the pipe core, and large scale instabilities along the shear layers and the pipe wall.

INTRODUCTION

Confined turbulent swirling flows are commonly encountered in industrial devices such as gas turbine combustors, combustion engines, turbomachine outlets and hydraulic turbine draft tube. Such flows are characterized by several striking features including collapse, vortex breakdown, hysteresis and axisymmetry breaking (Shtern and Hussain 1999). Vortex breakdown refers to a catastrophic structural disturbance in the core of an intense slender vortex characterized by the formation of an internal stagnation point on the vortex axis, followed by reversed flow in a region of limited axial extent. The characteristic of various breakdown states in the swirling flows depends on the swirl number S_r , defined as the ratio of axial fluxes of swirl and linear momentum divided by a characteristic radius, and Reynolds number Re . The characteristic forms of vortex breakdown

that dominate at high Re are the bubble and the spiral modes (Leibovich 1984). The addition of a sufficiently high degree of swirl to the flow into a circular pipe produces a limited region of reversed flow. Such a vortex breakdown represents a zone of transition from a supercritical to a subcritical flow state (Escudier 1987). Dellenback et al. (1988) observed experimentally that break of axial symmetry and onset of unsteadiness and three-dimensionality tend to occur for low swirl levels. As the swirl is increased, however, to moderate levels the flow becomes axisymmetric with on-axis recirculation marking the onset of bubble-type vortex breakdown. The specific mode of vortex breakdown that emerges in a turbulent flow is sensitive to both the Re and the local turbulence properties. Modes that have been observed experimentally at high Re include the conical, double-helix, spiral and bubble-type vortex breakdown (Sarpkaya 1995).

Although these striking features have been observed in several natural and technical flows, they are far from being well understood. The main difficulties arise from the large number of control parameters involved and the sensitivity of the swirling flow to external disturbances. Direct numerical simulations (DNS) of such flows are subject to the same problems, in addition to technical difficulties associated with complex flows and boundary conditions and grid resolution limitations at high Reynolds numbers. Large eddy simulation (LES) is a particularly suitable approach to investigate the generation and evolution of coherent structures in turbulent swirling flows (Schlüter et al. 2004; Wang et al. 2004, García-Villalba et al. 2006), but most of such simulations still focus on confined flows at moderate $Re \sim 10^4$ or unconfined swirling flows. Unsteady Reynolds-averaged Navier-Stokes (URANS) models provide a viable alternative for engineering computations of swirling flows at practical Re and in complex geometrical configurations. A number of such URANS computations with turbulence closures ranging from the linear eddy viscosity model to the second-moment closure models (Chen and Lin 1999; Jakirlić et al. 2002; Wegner et al. 2004, Gupta and Kumar 2007). URANS computations with the second-moment models or the RNG $k - \epsilon$ model are superior to conventional eddy viscosity models, such as the standard $k - \epsilon$ model, and reproduce the mean flow patterns in acceptable agreement with the experimental measurements and/or DNS or LES results. These simulations also reveal that significant challenges still remain in predicting accurately unsteady flow features and turbu-

lence statistics, such as the energy contained in the coherent motion of the precessing vortex core (Chen and Lin 1999; Jakirlić et al. 2002; Wegner et al. 2004). Detached-eddy simulation (DES) is a promising hybrid RANS/LES strategy capable of simulating internal flows dominated by large scale detached eddies at practical Reynolds number. The method aims at entrusting the boundary layer to RANS while the detached eddies in separated regions are resolved using LES. DES thus attempts to capitalize on the strengths of RANS and LES; the RANS region of a DES comprises the entire boundary layer with the remainder of the flow been treated in the LES mode using a subgrid model. DES predictions of massively separated flows, for which the technique was originally designed, are typically superior to those achieved using RANS models, especially in terms of the three-dimensional and time-dependent features of the flow (Fröhlich and von Terzi 2008; Spalart 2009).

For the turbulent swirling flow of Dellenback et al. (1988) several numerical works have been reported in the literature. Guo et al. (2001) carried out a URANS computation with the $k - \epsilon$ turbulence model at $Re = 1 \times 10^5$ (at the inlet) for S_r ranging from 0 to 0.48. Schlüter et al. (2004) performed LES computation of the swirling flow at Re of 3×10^4 for a range of swirl numbers from 0 to 0.6. In both computations, the inlet conditions are specified $0.5D$ (the pipe diameter) upstream of the expansion, where the flow might still be dominated by low-frequency, large-scale meandering of the vortex core especially at high swirl levels. To improve the solution accuracy of such simulations, the prescribed, periodic, turbulent inflow conditions with/without random fluctuations are often used, which yield acceptable predictions at moderate Reynolds numbers (Schlüter et al. 2004; Wang et al. 2004). However, the periodic inflow conditions assumes that the flow is steady in the mean (Schlüter et al. 2004) and the nonphysical random fluctuations imposed at the inlet plane decay quickly (Wang et al. 2004).

We report DES of the swirling flows studied experimentally by Dellenback et al. (1988) at $Re = 3.0 \times 10^4$ and 1.0×10^5 . We demonstrate that for accurate simulations the computational domain should start at a plane sufficiently far upstream of the expansion where the low-frequency large-scale meandering of the vortex core is not significant. This is followed by the presentation of a comparative study of the numerical results and the experimental measurements in terms of mean flow and turbulence statistics. Subsequently, various visualizations of the computed instantaneous coherent structures are used to elucidate the physics of the confined turbulent swirling flows at both applied Reynolds numbers. Finally, conclusions are drawn.

NUMERICAL METHODS

The governing equations are the three-dimensional, unsteady, incompressible, Reynolds-averaged Navier-Stokes (URANS) equations. Turbulence closure is achieved via the DES approach, which is a hybrid URANS/LES modeling strategy proposed by Spalart et al. (1997). The standard form of DES is based on the Spalart-Allmaras (S-A) one-equation eddy viscosity model (Spalart and Allmaras 1994), which solves a single transport equation for a working variable $\tilde{\nu}$ that is related to the turbulent viscosity ν_t . To alleviate the well known shortcoming of the standard DES, namely that of premature laminar-like flow separation, we employ an adjusted DES model Spalart et al. (2006) to ensure that a URANS layer is always present near the wall regardless of the local grid spacing. The

equations are transformed in generalized curvilinear coordinates and formulated in strong-conservation form are solved using a dual-time-stepping artificial compressibility (AC) iteration scheme. The AC form of the governing equations is discretized using a second-order-accurate finite-volume method on the non-staggered computational grid. The convective terms are discretized using the second-order accurate, upwind-biased QUICK scheme, and central differencing is employed for the pressure gradients, viscous fluxes and source terms in the turbulence equation. The third-order, fourth-difference artificial dissipation method of Sotiropoulos and Adballah (1991) is employed for the pressure to eliminate odd-even decoupling of the pressure field. The physical time derivatives are discretized with three-point-backward, Euler-implicit temporal-integration scheme. The discrete equations are marched in time to advance the solution to the next time step by adopting the dual-time-stepping method. The system of equations is integrated in pseudo time using the pressure-based implicit preconditioner (Paik et al. 2005) enhanced with local-time-stepping and V-cycle multigrid acceleration. The computational domain is discretized using the domain-decomposition approach with structured, overset grids. We apply a set of characteristics-based, non-reflecting boundary conditions at the outlet of the computational domain to allow complex vortical structures to exit the domain without distortion. The numerical method has been extensively evaluated for calculating various turbulent shear flows in complex geometrical configurations (Paik et al. 2005, 2007, 2009). For a detailed description of the numerical method the reader is referred to Paik et al. (2005). The code has been parallelized with MPI and run on a high performance computing cluster in the University of Minnesota Supercomputing Institute (MSI).

COMPUTATIONAL DETAILS

We simulate turbulent swirling flows through a sudden expansion at $Re = 3.0 \times 10^4$ and 1.0×10^5 , based on the diameter of the upstream tube D and the bulk velocity, which corresponds to the experiments of Dellenback et al. (1988). The applied swirl numbers S_r , the ratio of axial fluxes of angular momentum and axial momentum divided by a characteristic radius, range from 0.17 to 1.23. In the experiments, the sudden expansion was $15D$ downstream of the swirl generator, the expansion ratio D_2/D was 1.94 and the length of downstream tube was $20.47D$. Experimental measurements of axial and tangential components of mean velocity and root-mean-square (RMS) of turbulence levels were carried out by Dellenback et al. (1988) at several cross-sections downstream of the sudden expansion at various Re and S_r . For each set of measurements there are two profiles upstream of the expansion, $x = -2.0$ and -0.5 , which can be used as the inflow condition for the numerical simulations. The computational mesh discretized by domain decomposition with 4 overset grids and the coordinate system for the swirling flow are depicted in Figure 1. The total number of grid nodes, computational time steps for each application case are summarized in Table 1.

Dellenback et al. (1988) reported large influence of the downstream flow on the $x = -0.5$ profiles for all supercritical-swirl cases in the experiments. The influence is especially strong on the turbulence intensities whose magnitudes and distributions are changed dramatically as far upstream as $x = -2.0$. The turbulence intensities continue to be highly non-isotropic in the downstream tube for all the supercritical-swirl flows (Dellenback et al. 1988). Since the profiles of

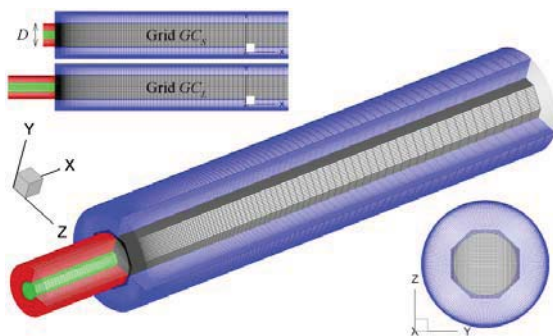


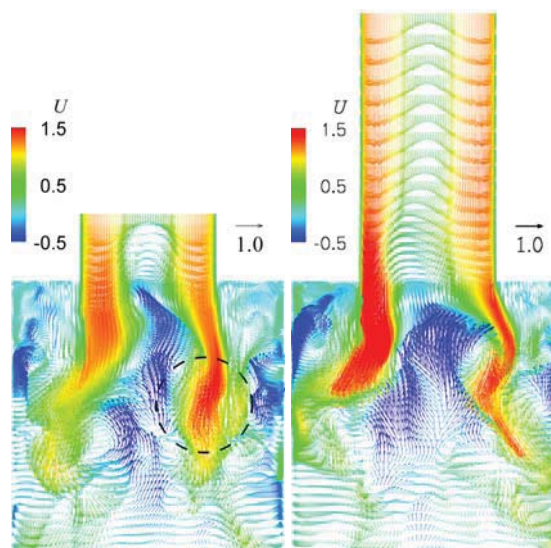
Figure 1: Computational grid and coordinate system.

Table 1: Summary of numerical configurations

Mesh	L_{Domain}	Nodes	Δt	Application
C_S	$0.5D+10D$	1,653,874	0.015	3×10^4
C_L	$2.0D+10D$	1,779,694	0.015	$3 \times 10^4, 1 \times 10^5$
$F1_L$	$2.0D+10D$	5,799,080	0.01	1×10^5
$F2_L$	$2.0D+10D$	7,915,880	0.01	1×10^5

both mean flow and turbulence intensities are significantly altered at these locations, the location of the inlet plane should be carefully selected. We employ two different meshes with upstream tubes of different lengths to elucidate the effect of the location of inlet plane on the flow downstream of the expansion. That is, the subscripts S and L in mesh names stand for computational domains with the short and long upstream tube starting at $x = -0.5$ and -2.0 , respectively. At each inlet plane, the inflow conditions of velocity components are prescribed using the experimental measurements (Dellenback et al. 1988). The eddy viscosity and the turbulence working variable $\tilde{\nu}$ required by the DES model at the inlet are pre-calculated using the mixing-length prescription of Norris and Reynolds (1975) and the measured turbulence intensity (Dellenback et al. 1988). The outlet boundary is placed at $x = 10D$ where the non-reflecting characteristic boundary conditions are applied. No-slip boundary conditions are applied on the pipe wall.

To examine the grid sensitivity of the computed solutions, in addition to the coarse grid simulations we also carry out numerical simulation for the $Re = 1.0 \times 10^5$ case on two finer meshes. One mesh is referred to as $F1_L$ is refined by a factor of $3/2$ in each direction and the other referred to $F2_L$ is further refined especially near the inlet and outlet boundaries by adding several grid nodes only in the axial direction. The first grid node off of all solid walls has been left unchanged on all grids and is located at $y^+ \leq 1.0$ everywhere. Numerical simulations are carried out using non-dimensional physical time steps of $\Delta t = 0.015$ and 0.01 for the computations on the coarse (C_S and C_L) and fine ($F1_L$ and $F2_L$) grids, respectively. Though the total number of grid nodes in the C_S and C_L meshes are similar to that used in a previous LES of Schüter et al. (2004), grid resolution near the wall and the center of computational domains is different from each other. That is, the cell size near the wall upstream of the expansion was about $y^+ = 25$ in the LES of Schüter et al. (2004) while the first node off the wall locates at $y^+ \leq 1$ everywhere in our computations. Given the similar number of grid nodes, therefore, the grid spacings near the center of our computational domains are considerably coarser than that used in the previous compu-

Figure 2: Effect of inlet conditions on the flow after expansion: instantaneous velocity vectors at the plane of symmetry computed on (left) C_S and (right) C_L meshes at $Re = 3.0 \times 10^4$ and $Sr = 0.60$.

tations (Schüter et al. 2004).

RESULTS AND DISCUSSION

In this section, we first demonstrate the need to prescribe inflow boundary conditions at a plane located sufficiently far upstream of the expansion where the low-frequency large-scale meandering of the vortex core is not significant. The effect of the inlet location on the flow is illustrated in Figure 2 which shows instantaneous velocity vector fields computed at the plane of symmetry on the short (C_S) and the long (C_L) domain meshes. The solution computed on the C_L mesh reveals that the vortex breakdown bubble exhibits considerably more intense unsteadiness and extends to about $2.25D$ downstream of the expansion. Video animations downstream of the bubble, composed using instantaneous snapshots, along with the computed mean flow quantities (see Figure 3) further show that although fluid on the tube axis is mostly stagnant in the mean, it is quite unsteady, sometimes showing a tendency to drift in seemingly random manner either upstream or downstream. This result is consistent with the experimental observation of Dellenback et al. (1988). The solution computed on the C_L mesh also depicts the vortex core with the large-scale meandering upstream of the expansion and its breakdown downstream of the pipe expansion. In the C_S computation, on the other hand, the vortex core meandering is completely suppressed, as shown in Figure 2, which results in the formation of a spurious bubble-type vortex breakdown just downstream of the inlet and the underestimation of the spreading rate of the jet (see the dash-line circle in Figure 2). Consequently, the jet core computed on the C_S mesh penetrates farther downstream than that computed on the C_L mesh. This result is consistent with the previous works by Schlüter et al. (2004) who further demonstrated that the simple turbulent inflow conditions with imposing random fluctuations essentially yields the same results and can not improve the solution accuracy (also see Wang et al. (2004) for the same results at a different geometrical configuration).

The comparison of the numerical results obtained on the

C_S and C_L domains and the experimental measurements (Dellenback et al. 1988) at $Re = 3.0 \times 10^4$ and $S_r = 0.60$ is shown in Figure 3 in terms of mean flow and turbulence intensity profiles. It is evident in these figures that significant discrepancies between the two domain solutions are observed in terms of the axial mean velocity profiles and both axial and tangential RMS profiles downstream of the expansion. The artificial suppression of the precession of the vortex core due to the steady inflow conditions causes the strong jet flow and distorts the axial velocity and turbulence intensity profiles downstream of the expansion (see blue line at $0.5 \leq x \leq 1.0$). Figure 3 demonstrates that the specification of inflow conditions sufficiently upstream of the expansion so that the low-frequency, large-scale precession of the vortex core is not spuriously suppressed is prerequisite for reproducing the mean flow profiles as well as turbulence statistics with good accuracy.

The numerical solutions obtained at $Re = 1.0 \times 10^5$ and $S_r = 0.74$, which are not included in this paper due to space limitation, lead to the same conclusion derived from Figure 3. These solutions further demonstrate that, as the Re increases, it is necessary to refine the computational mesh to capture the mean flow and the turbulent intensity with good accuracy in the whole domain. This result is supported by Figure 4 which shows the modeled and total (modeled+total) Reynolds stress $-\overline{u'w'}$ computed at the plane of symmetry on the fine meshes (C_L and $F2_L$ for at $Re=3.0 \times 10^4$ and $Re=1.0 \times 10^5$, respectively). This figure illustrates that the Reynolds stress modeled by the subgrid model is essentially negligible and most of turbulence energy has been fully resolved in the fine mesh simulation.

Figure 5 shows the power spectra of the axial velocity computed at two points in the flows at $Re=3.0 \times 10^4$ and $Re=1.0 \times 10^5$: 1) a point $0.5D$ downstream of the expansion where the flow is characterized by the existence of the precessing vortex core with a dominant frequency of about 0.7; and 2) a point at $2.0D$ downstream of the expansion where our solution yields several harmonics associated with the breakdown of the vortex core to small structures and the interaction of these structures and the pipe wall. These features of the computed flow are in good agreement with the measurements of Dellenback et al. (1988). Our simulation also yields velocity spectra that exhibit a clear $-5/3$ power law inertial subrange at both locations.

Various visualizations of the computed instantaneous coherent structures are used to elucidate the physics of the confined turbulent swirling flows at both simulated Re . To identify the coherent structures in the computed flow fields, we first employ the so-called q -criterion defined by $q = \frac{1}{2} (\|\Omega^2\| - \|\mathbf{S}^2\|)$ where $\|\cdot\|$ is the Euclidean matrix norm and Ω and \mathbf{S} denote the symmetric and antisymmetric parts of the velocity gradient, respectively (Hunt et al. 1988). Figure depicts the onset of vortex breakdown for $Re=3.0 \times 10^4$ and $S_r = 0.60$ and $Re=1.0 \times 10^5$ and $S_r = 0.74$. The instantaneous iso-surface of q -criterion ($=0.8$) shown in Figure 7 illustrates that strong vortical structures develop along the centerline and relatively weak vortices are sustained along near the pipe wall in the entire length of the downstream pipe. The former are obviously associated with the on-axis, elongated pocket of recirculating flow on the tube centerline, as shown with the iso-surface of a small negative value of axial velocity in Figure 7, while the latter are presumably linked to the instability of the flow along the concave wall boundary layer (made visible in the limiting streamline plot).

Figure 8 shows streak-line visualization of the turbulent

vortex breakdown using Lagrangian tracking of particles released at four equidistant azimuthal positions near the center at the inlet plane. This figure clearly depicts that the dependence of the vortex breakdown phenomenon on the swirl number of the flow. At the low S_r the vortex core breaks down far downstream near $x = 4.0$ while the breakdown location moves upstream as S_r increases. At the highest S_r ($=1.23$) particles are scattered as soon as they released, as shown in Figure 8. At the same time, it should be noted that vortex breakdown in the upstream pipe is somewhat attributed to the fact that for the highest swirl case the location of the inlet plane is apparently not far upstream to completely avoid the artificial suppression of the precession of the vortex core.

CONCLUSIONS

Numerical results show that for swirling flow in a sudden expansion at high Re and S_r , the low-frequency, large-scale meandering of the vortex core reaches far upstream of the expansion. Thus careful specification of inflow conditions along with proper grid refinement are crucial prerequisites for resolving the mean flow as well as turbulence statistics over the entire computational domain. The solutions computed on the refined long domain appear to be in excellent agreement with the experimental measurements (Dellenback et al. 1988) in terms of mean flow and turbulence intensity. Using the flow visualization techniques, we discussed the structure and temporal dynamics of the turbulent vortex breakdown and other large scale instabilities that occur in the shear layers and along the pipe wall over a range of swirl intensities. A more detailed discussion of the computed results and underlying flow physics will be presented in a journal publication, which is currently in preparation.

ACKNOWLEDGMENTS

This work was supported by NSF Grants EAR-0120914 (as part of the National Center for Earth-surface Dynamics) and EAR-0738726, and a grant (Code#06 CTIP B-01) from the Ministry of Land, Transport and Maritime Affairs of Korean Government. Computational resources were provided by the University of Minnesota Supercomputing Institute.

REFERENCES

- Chen, J. C. and Lin, C. A., 1999, "Computations of Strongly Swirling Flows with Second-Moment Closures", *Int. J. Numer. Meth. Fluids*, Vol. 30, pp. 493-508.
- Dellenback, P. A., Metzger, D. E., and Neitzel, G. P., 1989, "Measurements in Turbulent Swirling Flow through an Abrupt Axisymmetric Expansion", *AIAA Journal*, Vol. 26, No. 6, pp. 669-681.
- Escudier, M., 1987, "Confined Vortices in Flow Machinery", *Annu. Rev. Fluid Mech.*, Vol. 19, pp. 27-52.
- Fröhlich, J. and von Terzi, D., 2008, "Hybrid LES/RANS methods for the simulation of turbulent flows", *Progress in Aerospace Sciences*, Vol. 44, pp. 349-377.
- García-Villalba, M., Fröhlich, J., and Rodi, W., 2006, "Identification and Analysis of Coherent Structures in the Near Field of a Turbulent Unconfined Annual Swirling Jet Using Large Eddy Simulation", *Physics of Fluids*, Vol. 18, 055103.
- Guo, B., Langrish, T. A. G., and Fletcher, D. F., 2001, "Simulation of Turbulent Swirling Flow in an Axisymmetric Sudden Expansion", *AIAA Journal*, Vol. 39, No. 1, pp.

96-102.

Gupta, A. and Kumar, R., 2007, "Three-Dimensional Turbulent Swirling Flow in a Cylinder: Experiments and Computations", *International Journal of Heat Fluid Flow*, Vol. 28, pp. 249-261.

Hunt, J. C. R., Wary, A. A. and Moin, P., 1988, "Eddies, Stream and Convergence Zones in Turbulent Flows", Center of Turbulence Research, CTR-S88, pp. 193-208.

Jakirlić, S., Hanjalić, K., and Tropea, C., 2002, "Modeling Rotating and Swirling Turbulent Flows: A Perpetual Challenge", *AIAA Journal*, Vol. 40, No. 10, pp. 1984-1996.

Leibovich, S., 1984, "Vortex Stability and Breakdown: Survey and Extension", *AIAA Journal*, Vol. 22, pp. 1192-1206.

Norris, L. H., and Reynolds, W. C., 1975, "Turbulent Channel Flow with a Moving Wavy Boundary", *Report FM-10*, Dept. of Mech. Eng., Stanford University, Stanford, CA.

Paik, J., Sotiropoulos, F., and Sale, M. J., 2005, "Numerical Simulation of Swirling Flow in a Hydroturbine Draft Tube Using Unsteady Statistical Turbulence Models", *ASCE Journal of Hydraulic Engineering*, Vol. 131, No. 6, pp. 441-456.

Paik, J., Escauriaza, C., and Sotiropoulos, F., 2007, "On the Bi-Modal Dynamics of the Turbulent Horseshoe Vortex System in a Wing-Body Junction", *Physics of Fluids*, Vol. 19, No. 4, pp. 045107.

Paik, J., Sotiropoulos, F., and Porté-Agel, 2009, "Detached-Eddy Simulation of Flow around Two Wall-Mounted Cubes in Tandem", *Int. J. Heat Fluid Flow*, Vol. 30, pp. 286-305.

Sarpkaya, T., 1995, "Turbulent Vortex Breakdown", *Physics of Fluids*, Vol. 7, No. 10, pp. 2301-2303.

Schlüter, J. U., Pitsch, H., and Moin, P., 2004, "Large Eddy Simulation Inflow Conditions for Coupling with Reynolds-Averaged Flow Solvers", *AIAA Journal*, Vol. 42, No. 3, pp. 478-484.

Shtern, V. and Hussain, F., 1999, "Collapse, Symmetry, Breaking, and Hysteresis in Swirling Flow", *Annual Review of Fluid Mechanics*, Vol. 31, pp. 537-566.

Sotiropoulos, F., and Adballah, S., 1991, "The Discrete Continuity Equation in Primitive Variable Solutions of Incompressible Flow", *Journal of Computational Physics*, Vol. 95, pp. 212-227.

Spalart, P. R. and Allmaras, S. R., 1994, "A One-Equation Turbulence Model for Aerodynamic Flows", *La Recherche Aerospaciale*, Vol. 1, pp. 5-21.

Spalart, P. R., Jou, W. H., Strelets, M., and Allmaras, S. R., 1997, "Comments on the Feasibility of LES for Wings and on a Hybrid RANS/LES Approach", In: Liu, C., Liu, Z. Eds., *Advances in DNS/LES*, Greyden Press, Columbus, OH.

Spalart, P., Deck, S., Shur, M., Squires, K., Strelets, M., Travin, A., 2006, "A New Version of Detached-Eddy Simulation, Resistant to Ambiguous Grid Densities", *Theor. Comput. Fluid Dyn.*, Vol. 20, No. 3, pp. 181-195.

Spalart, P., 2009, "Detached-Eddy Simulation", *Annu. Rev. Fluid Mech.*, Vol. 41, pp. 181-202.

Wang, P., Bai, X. S., Wessman, M., and Klingmann, J., 2004, "Large Eddy Simulation and Experimental Studies of a Confined Turbulent Swirling Flow", *Physics of Fluids*, Vol. 16, No. 9, pp. 3306-3324.

Wegner, B., Maltsev, A., Schneider, C., Sadiki, A., Dreizler, A., and Janicka, J., 2004, "Assessment of Unsteady RANS in Predicting Swirl Flow Instability Based on LES and Experiments", *International Journal of Heat and Fluid Flow*, Vol. 25, pp. 528-536.

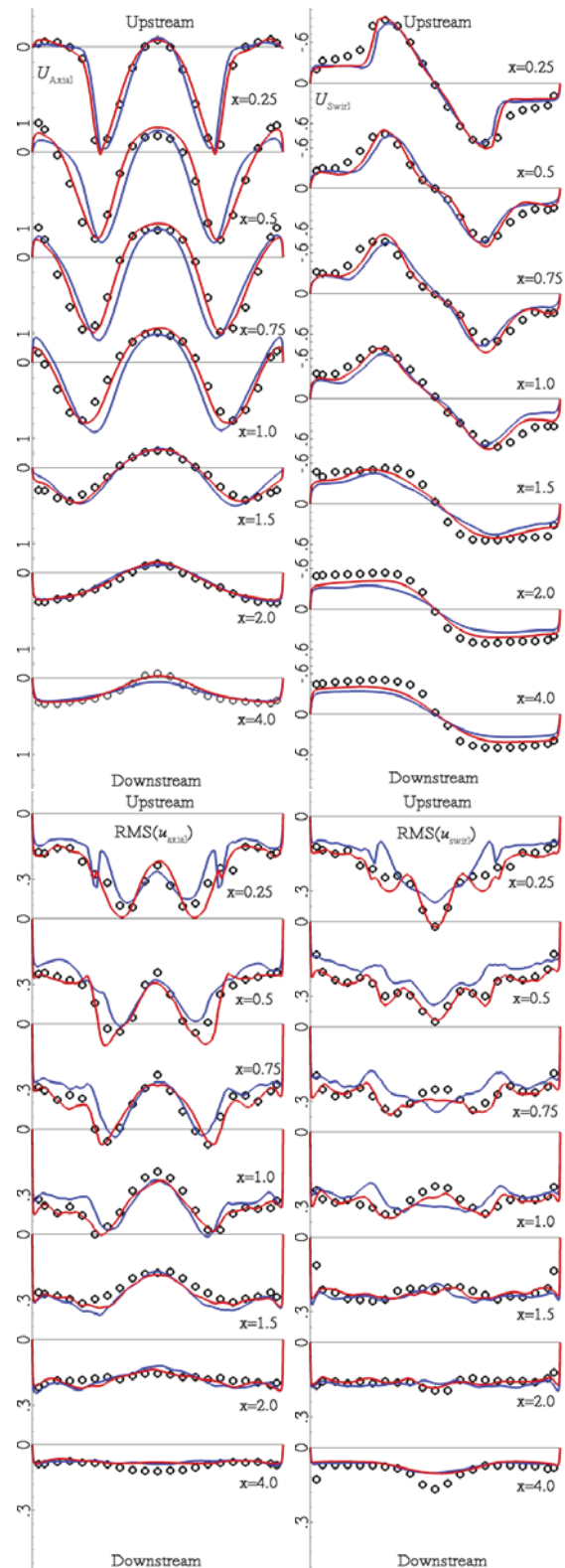


Figure 3: Comparison of axial mean velocity, tangential mean velocity, RMS of axial velocity fluctuations and RMS of tangential velocity fluctuations computed on C_S (blue line) and C_L (red line) meshes with the measurements (circles) at $Re = 3.0 \times 10^4$ and $S_r = 0.60$.

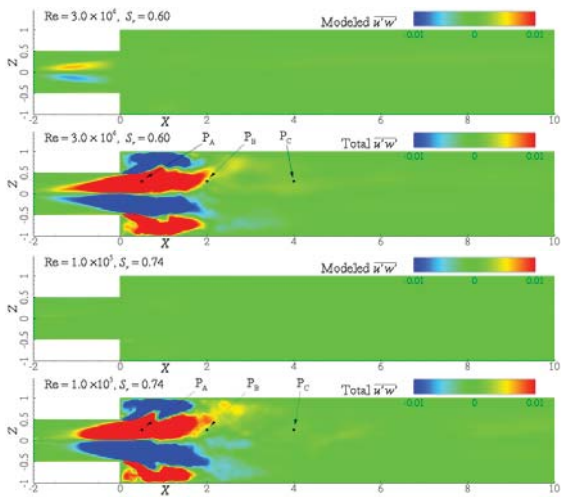


Figure 4: Modeled and total (modeled+resolved) Reynolds shear stress $u'w'$

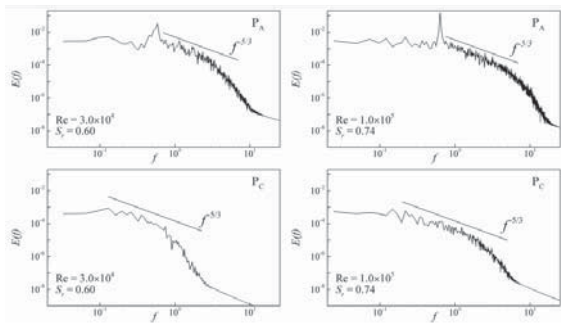


Figure 5: Power spectral density of streamwise velocity computed at two selected streamwise locations (see Figure 4 for locations of P_A , P_B and P_C)

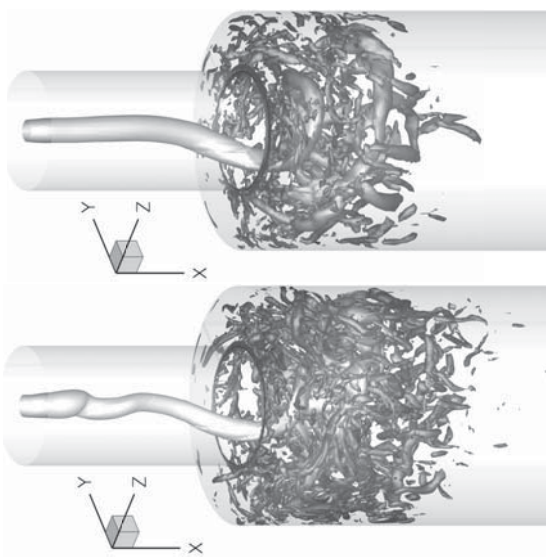


Figure 6: Vortex breakdown visualized by instantaneous iso-surface of q -criterion ($= 50$) colored by pressure (white, low and black, high) computed at (left) $Re = 3.0 \times 10^4$ and $S_r = 0.60$, and (right) $Re = 1 \times 10^5$, $S_r = 0.74$.

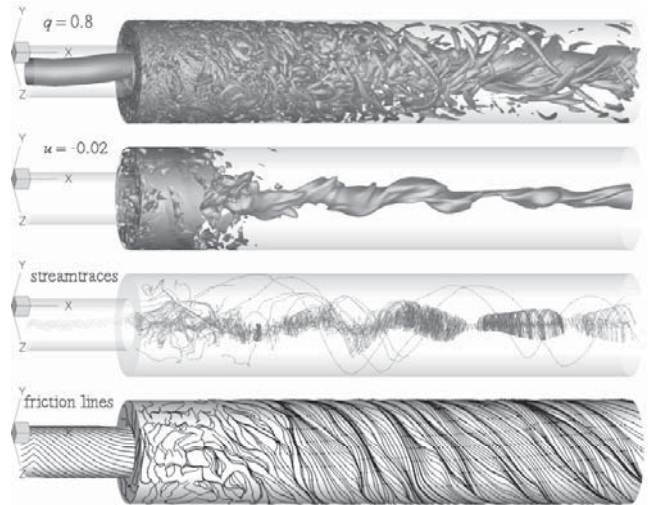


Figure 7: Swirling flow visualized by instantaneous iso-surface of q ($=0.8$), iso-surface of a negative axial velocity ($=-0.02$), 3D streamtraces colored by pressure (white, low; black, high) and friction lines: solutions on the $F2_L$ mesh at $Re = 1 \times 10^5$, $S_r = 0.74$.

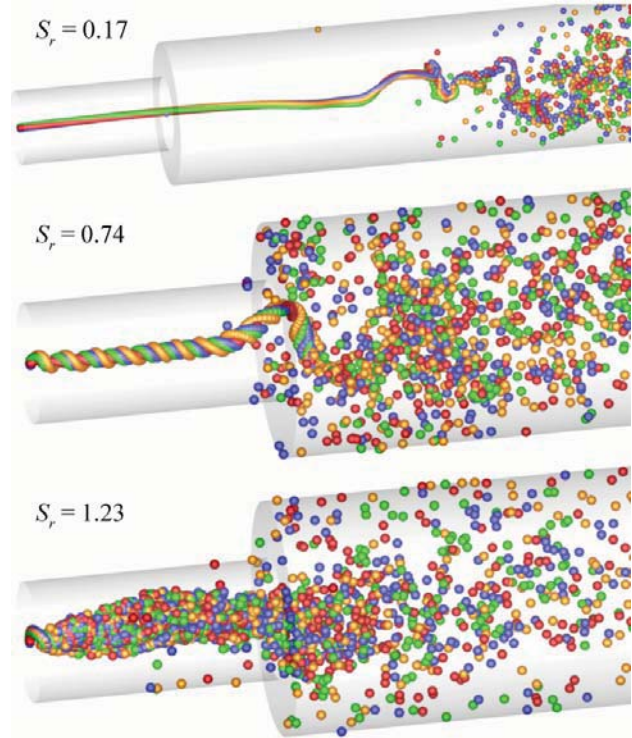


Figure 8: Streakline visualization of the turbulent vortex breakdown identified by Lagrangian tracking of fluid particles released near the center of the inlet plane at $Re = 1 \times 10^5$ and at different swirl numbers